

Electronic Structure of Bilayer Graphene: A Real-space Green's Function Study

Z.F.Wang,¹ Qunxiang Li,^{1,*} Haibin Su,² Xiaoping Wang,¹

Q.W.Shi,^{1,†} Jie Chen,³ Jinlong Yang,¹ and J.G.Hou¹

¹*Hefei National Laboratory for Physical Sciences at Microscale,*

University of Science and Technology of China,

Hefei, Anhui 230026, People's Republic of China

²*School of Materials Science and Engineering,*

Nanyang Technological University, 50 Nanyang Avenue, 639798, Singapore

³*Electrical and Computer Engineering,*

University of Alberta, AB T6G 2V4, Canada

(Dated: February 6, 2008)

Abstract

In this paper, a real-space analytical expression for the free Green's function (propagator) of bilayer graphene is derived based on the effective-mass approximation. Green's function displays highly spatial anisotropy with three-fold rotational symmetry. The calculated local density of states (LDOS) of a perfect bilayer graphene produces the main features of the observed scanning tunneling microscopy (STM) images of graphite at low bias voltage. Some predicted features of the LDOS can be verified by STM measurements. In addition, we also calculate the LDOS of bilayer graphene with vacancies by using the multiple-scattering theory (scatterings are localized around the vacancy of bilayer graphene). We observe that the interference patterns are determined mainly by the intrinsic properties of the propagator and the symmetry of the vacancies.

PACS numbers: 73.61Wp, 61.72.Ji, 68.37.Ef

I. INTRODUCTION

Since Novoselov *et al.* fabricated ultra-thin monolayer graphite devices,¹ the electronic properties of a graphite monolayer (graphene) have attracted a great deal of research interest due to the Dirac-type spectrum of charge carriers in its gap-less semiconductor material. Many interesting properties of single-layer graphene, such as the Landau quantization, the defect-induced localization, and spin current states, have been studied experimentally and theoretically by several research groups.^{2,3,4,5,6,7} These non-orthodox properties, including massless Dirac fermions around the Dirac points in the first Brillouin zone, result from graphene's particular band structure.

Recent research attention has focused on the electronic structure of bilayer and multilayer graphene.^{8,9,10,11,12,13,14} Studies have shown that a bilayer graphene has some unexpected properties.¹¹ For example, a bilayer graphene shows anomalies in its integer quantum Hall effect and in its minimal conductivity on the order of e^2/h . The common and distinctive electronic features of single-layer and bilayer graphene are highlighted in Ref.[15]. Charge carriers in a bilayer graphene are mainly quasiparticles with a finite density of states at zero energy and they behave similar to conventional non-relativistic electrons. Like the relativistic particles or quasiparticles in single-layer graphene, we can describe these quasiparticles by using spinor wavefunctions. Although these 'massive chiral fermions' do not exist in the field theory, their existence in condensed-matter physics offers a unique opportunity to investigate the importance of chirality and to solve the relativistic tunneling problem.

The unusual physical properties of bilayer graphene are attributed to two key factors. (i) The relatively weak inter-layer coupling. Bilayer graphene inherits some properties from single-layer graphene material, such as the existence of Dirac points in the first Brillouin zone and the degeneracy of electron and hole bands. (ii) The special geometry of bilayer graphene with the Bernal stacking (A-B stacking) between adjacent graphene layers. There are two kinds of nonequivalent sites (A and B) in each layer as shown in Fig.1(a) and 1(b). Experimental scanning tunneling microscopy (STM) graphite images at low bias voltage have verified that only site B is visible and exhibits a triangular structure. In addition, the orbital overlap coupling between two adjacent layers is contributed mainly by the carbon orbitals at site A.^{16,17,18} To date, few analytical studies that attempt to uncover the unique electronic properties of the bilayer graphene have been done.¹²

In this paper, we first develop an analytical formula of electronic structure in a bilayer graphene with the Bernal stacking based on real-space free Green's function (propagator) and the effective-mass approximation. We observe that the physical properties of the bilayer graphene are closely related to its propagator and the bilayer graphene behaves similar to a massive chiral Fermions system. Since the local density of states (LDOS) can be measured by STM, we then compute the LDOS of graphene in various forms based on Green's function explicitly. Finally, we highlight the impact of vacancies' patterns (in terms of their geometry and symmetry of the computed LDOS) on interferences in STM pictures.

II. A REAL-SPACE GREEN'S FUNCTION AND ELECTRONIC STRUCTURE OF PERFECT BILAYER GRAPHENE

In what follows, we derive the analytical expression of the free Green's function for bilayer graphene in real space based on the effective-mass approximation. Bilayer graphene consists of two hexagonal lattice layers coupled by the Bernal stacking as shown in Fig.1 (a) and (b). In each layer, there are two nonequivalent sites, A and B. Type-A atoms have direct neighbors in their adjacent layer, but type-B atoms do not and locate at hollow sites. We assume that there is one valence electron per carbon atom in a bilayer graphene. Provided that the difference between wavefunctions orthogonal to the graphene plane can be neglected, the bilayer graphene can be modeled as an effective two-dimensional system. Since the physical properties of graphene are determined by π bands near the Dirac point, only the contribution from the π band is considered in this paper. We further limit our analysis by considering only the nearest interactions of the graphene's p_z orbitals. The tight-binding Hamiltonian of the bilayer graphene is

$$\begin{aligned}
H = & \sum_i \epsilon_{2p} (|i\rangle_{11}\langle i| + |i\rangle_{22}\langle i|) \\
& + V_1 \sum_{\langle ij \rangle} (|i\rangle_{11}\langle j| + |i\rangle_{22}\langle j| + h.c.) \\
& + V_2 \sum_{\langle ij \rangle} (|i\rangle_{12}\langle j| + h.c.)
\end{aligned} \tag{1}$$

where $\langle \mathbf{r}|i\rangle_l$, $l = (1, 2)$ is a wavefunction at site i at layer l . ϵ_{2p} is the on-site energy, V_1 is the nearest hopping parameter within the layer and V_2 is the nearest hopping parameter

between two layers. Our presented calculations are conducted with $\epsilon_{2p} = 0\text{eV}$, $V_1 = -3.0\text{eV}$ and $V_2 = 0.4\text{eV}$.

The Bloch orbits for two nonequivalent sites, A and B, are written as $|k_A\rangle_l = \frac{1}{\sqrt{N}} \sum_{j_A} e^{i\mathbf{k}\cdot\mathbf{r}_{jA}} |j_A\rangle_l$, $|k_B\rangle_l = \frac{1}{\sqrt{N}} \sum_{j_B} e^{i\mathbf{k}\cdot\mathbf{r}_{jB}} |j_B\rangle_l$. The summation covers all sites A and B on layer l . \mathbf{r}_A and \mathbf{r}_B denote the real-space coordinates of sites A and B, respectively. Here, N is the number of unit cells in the crystal. The Hamiltonian can be rewritten as

$$H = \begin{pmatrix} \epsilon_{2p} & V_1\mu^* & V_2 & 0 \\ V_1\mu & \epsilon_{2p} & 0 & 0 \\ V_2 & 0 & \epsilon_{2p} & V_1\mu \\ 0 & 0 & V_1\mu^* & \epsilon_{2p} \end{pmatrix}, \quad (2)$$

where $\mu = e^{ik_y a} + e^{i(-\frac{\sqrt{3}ak_x}{2} - \frac{ak_y}{2})} + e^{i(\frac{\sqrt{3}ak_x}{2} - \frac{ak_y}{2})}$ and $a = 1.42\text{\AA}$ is the c-c bond length. By defining the retarded Green's function as, $G_0^{ret} = 1/(\epsilon - H + i\eta)$, where η is an infinitesimal quantity, we obtain the reciprocal space Green's function for bilayer graphene

$$G_0^{ret}(\mathbf{k}, \epsilon) = \frac{1}{\Delta} \begin{pmatrix} t(t^2 - V_1^2\mu\mu^*) & V_1\mu^*(t^2 - V_1^2\mu\mu^*) & t^2V_2 & tV_1V_2\mu \\ V_1\mu(t^2 - V_1^2\mu\mu^*) & t(t^2 - V_1^2\mu\mu^* - V_2^2) & tV_1V_2\mu & V_1^2V_2\mu^2 \\ t^2V_2 & tV_1V_2\mu^* & t(t^2 - V_1^2\mu\mu^*) & V_1\mu(t^2 - V_1^2\mu\mu^*) \\ tV_1V_2\mu^* & V_1^2V_2\mu^{*2} & V_1\mu^*(t^2 - V_1^2\mu\mu^*) & t(t^2 - V_1^2\mu\mu^* - V_2^2) \end{pmatrix} \quad (3)$$

where $\Delta = (t^2 - V_1^2\mu\mu^* - tV_2)(t^2 - V_1^2\mu\mu^* + tV_2)$ and $t = \epsilon - \epsilon_{2p} + i\eta$. From $\Delta = 0$, the dispersion relation is expressed as $\epsilon = \pm \frac{V_2}{2} \pm \sqrt{(\gamma k)^2 + (\frac{V_2}{2})^2}$ with $\gamma = 3aV_1/2$, which is consistent with the previous theoretical result.¹²

The real-space Green's function of the bilayer graphene can be derived by taking the Fourier transform of $G_0^{ret}(\mathbf{k}, \epsilon)$. For simplicity, these calculations are carried out around six corners in the first Brillouin zone within the low-energy region based on the effective-mass approximation,. Six Dirac points can be divided into two equivalent sets of points, K^1, K^3, K^5 and K^2, K^4, K^6 , which are shown in Fig.1(c). They form two 360° integrals around K^1 and K^4 . By using the mathematical relation

$$e^{i\mathbf{k}\cdot(\mathbf{r}_\mu - \mathbf{r}'_\nu)} = J_0(k|\mathbf{r}_\mu - \mathbf{r}'_\nu|) + 2\sum_{n=1}^{\infty} i^n J_n(k|\mathbf{r}_\mu - \mathbf{r}'_\nu|) \cos(n\varphi_{r_\mu, r'_\nu}),$$

where $(\mu, \nu) = (A, B)$, φ_{r_μ, r'_ν} is the angle between \mathbf{k} and $\mathbf{r}_\mu - \mathbf{r}'_\nu$, and J_n is the type-I n -order Bessel function. We can simplify the real-space Green's function of the top layer ($l = 1$) to

$$\begin{aligned}
G_0^{ret}(\mathbf{r}_A, \mathbf{r}'_A, \varepsilon) &= \cos[\mathbf{K}^1 \cdot (\mathbf{r}_A - \mathbf{r}'_A)] \cdot F_1(|\mathbf{r}_A - \mathbf{r}'_A|, \varepsilon) \\
G_0^{ret}(\mathbf{r}_B, \mathbf{r}'_B, \varepsilon) &= \cos[\mathbf{K}^1 \cdot (\mathbf{r}_B - \mathbf{r}'_B)] \cdot F_2(|\mathbf{r}_B - \mathbf{r}'_B|, \varepsilon) \\
G_0^{ret}(\mathbf{r}_A, \mathbf{r}'_B, \varepsilon) &= \sin[\mathbf{K}^1 \cdot (\mathbf{r}_A - \mathbf{r}'_B) + \alpha_{r_A, r'_B}] \\
&\quad \cdot F_3(|\mathbf{r}_A - \mathbf{r}'_B|, \varepsilon) \\
G_0^{ret}(\mathbf{r}_B, \mathbf{r}'_A, \varepsilon) &= \sin[\mathbf{K}^1 \cdot (\mathbf{r}_B - \mathbf{r}'_A) - \alpha_{r_B, r'_A}] \\
&\quad \cdot F_3(|\mathbf{r}_B - \mathbf{r}'_A|, \varepsilon),
\end{aligned} \tag{4}$$

Here $\mathbf{K}^1 = (4\pi/3\sqrt{3}a, 0)$, $\cos\varphi_{r_\mu, r'_\nu} = \cos(\theta - \alpha_{r_\mu, r'_\nu})$, θ is the angle between the \mathbf{k} and x axis. α_{r_μ, r'_ν} is the angle between $\mathbf{r}_\mu - \mathbf{r}'_\nu$ and x axis. The definitions of F_1, F_2 , and F_3 are

$$\begin{aligned}
F_1(|\mathbf{r}_\mu - \mathbf{r}'_\nu|, \varepsilon) &= \frac{S}{\pi} \int_0^{k_c} dk k J_0(k|\mathbf{r}_\mu - \mathbf{r}'_\nu|) \\
&\quad \times \left[\frac{t}{t^2 - (\gamma k)^2 - tV_2} + \frac{t}{t^2 - (\gamma k)^2 + tV_2} \right], \\
F_2(|\mathbf{r}_\mu - \mathbf{r}'_\nu|, \varepsilon) &= \frac{S}{\pi} \int_0^{k_c} dk k J_0(k|\mathbf{r}_\mu - \mathbf{r}'_\nu|) \\
&\quad \times \left[\frac{t - V_2}{t^2 - (\gamma k)^2 - tV_2} + \frac{t + V_2}{t^2 - (\gamma k)^2 + tV_2} \right], \\
F_3(|\mathbf{r}_\mu - \mathbf{r}'_\nu|, \varepsilon) &= \frac{S}{\pi} \int_0^{k_c} dk k^2 J_1(k|\mathbf{r}_\mu - \mathbf{r}'_\nu|) \\
&\quad \times \left[\frac{\gamma}{t^2 - (\gamma k)^2 - tV_2} + \frac{\gamma}{t^2 - (\gamma k)^2 + tV_2} \right].
\end{aligned} \tag{5}$$

where $S = 3\sqrt{3}a^2/2$ is the area of the unit cell in real space and k_c is the cutoff wave vector. The corresponding cutoff wave length $2\pi/k_c$ is comparable to the lattice constant a . With the same approach in our previous work to solve electronic structure in the single-layer graphene, k_c is set to be $1.71/a$.¹⁹ From Eq.(4), it is clear that the real-space Green's function of the bilayer graphene is constructed by multiplying two terms. The first term is spatially anisotropic, which can be represented by sine and cosine functions determined from two nonequivalent sets of the Dirac points as shown in Fig.1(c). The second term including F_1 , F_2 or F_3 is spatially isotropic in real space and depends only on the distance between two sites.

Many physical properties of bilayer graphene can be deduced from this explicit expression. Interestingly, when $k_c \rightarrow \infty$, the functions, F_1, F_2 and F_3 , have simple analytical forms

$$\begin{aligned}
F_1(|\mathbf{r}_\mu - \mathbf{r}'_\nu|, \varepsilon) &= \frac{-S}{\pi\gamma^2} [tK_0(\frac{it_1}{\gamma}|\mathbf{r}_\mu - \mathbf{r}'_\nu|) \\
&\quad + tK_0(\frac{it_2}{\gamma}|\mathbf{r}_\mu - \mathbf{r}'_\nu|)], \\
F_2(|\mathbf{r}_\mu - \mathbf{r}'_\nu|, \varepsilon) &= \frac{-S}{\pi\gamma^2} [(t - V_2)K_0(\frac{it_1}{\gamma}|\mathbf{r}_\mu - \mathbf{r}'_\nu|) \\
&\quad + (t + V_2)K_0(\frac{it_2}{\gamma}|\mathbf{r}_\mu - \mathbf{r}'_\nu|)], \\
F_3(|\mathbf{r}_\mu - \mathbf{r}'_\nu|, \varepsilon) &= \frac{-S}{\pi\gamma^2} [it_1K_1(\frac{it_1}{\gamma}|\mathbf{r}_\mu - \mathbf{r}'_\nu|) \\
&\quad + it_2K_1(\frac{it_2}{\gamma}|\mathbf{r}_\mu - \mathbf{r}'_\nu|)], \tag{6}
\end{aligned}$$

where $t_1 = \sqrt{t^2 - tV_2}$ and $t_2 = \sqrt{t^2 + tV_2}$. K_0 and K_1 are the zero-th order and the first order terms of the type-I modified Bessel function, respectively. Compared with our previous study,¹⁹ the expressions of the Green's function derived here are the same as those of the single-layer graphene once the nearest hopping parameter between two layers (V_2) is set to zero. That is to say, it is straightforward to compare theoretical results of bilayer graphene with previous theoretical and experimental data of the monolayer graphene by setting $V_2 = 0$.¹⁹

Fig.2 shows the LDOS of bilayer graphene with $\varepsilon = -0.1$ eV. Here, the LDOS of site \mathbf{r}_μ is calculated by setting $\rho_0(\mathbf{r}_\mu, \varepsilon) = -\frac{1}{\pi} \text{Im} G_0^{\text{ret}}(\mathbf{r}_\mu, \mathbf{r}_\mu, \varepsilon)$. We can clearly observe the contrast between the LDOS at site A and that at site B. Site B is highlighted and forms a triangular lattice with three-fold symmetry. According to the Tersoff-Hamann model²⁰ which has been successfully used to explain experimental results,^{21,22} the STM image can be simulated using the LDOS of the sample surface. It is reasonable for us to compare the LDOS of bilayer graphene with previous experimental STM observations of graphite surfaces at low bias voltage (i.e. 0.3 V). Our calculated LDOS can clearly produce the main features as shown in several observed STM images reported in Ref.[16-18].

One direct approach to find the difference between bilayer and monolayer graphene is to study the LDOS at sites A and B for both monolayer and bilayer graphenes. Fig.3(a) and 3(b) present the LDOS of one carbon site (A or B) in the monolayer graphene and two sites (A and B) in the bilayer graphene, respectively. For a monolayer graphene, sites A and B are equivalent and thus only one curve of LDOS is shown in Fig.2(a). However,

these two sites are nonequivalent for a bilayer graphene. Fig.2(b), therefore, clearly shows that the LDOS of bilayer graphene at site B is greater than that at site A, when $|\varepsilon|$ is less than approximately 0.4 eV. This LDOS difference leads to the brighter spots at site-B as shown in Fig.2. When $|\varepsilon| > 0.4$ eV, the difference between the LDOS at sites A and B in the bilayer graphene gradually diminishes. This feature is easy to verify through STM dI/dV mapping at a relatively large bias voltage. For example, sites A and B can be both observed in STM dI/dV mapping with the applied bias voltage of 0.6 V. This phenomenon can also be elaborated by our analytic expression of Green's function.

The difference between the LDOS of site A and that of site B can be defined as

$$\begin{aligned}\Delta\rho_0(\varepsilon) &= -\frac{1}{\pi}\text{Im}[G_0^{ret}(\mathbf{r}_B, \mathbf{r}_B, \varepsilon) - G_0^{ret}(\mathbf{r}_A, \mathbf{r}_A, \varepsilon)] \\ &= -\frac{1}{\pi}\text{Im}[F_2(0, \varepsilon) - F_1(0, \varepsilon)].\end{aligned}\quad (7)$$

After some simple math operations, shown in Appendix Eq.(A-5) and Eq.(A-6), $\Delta\rho_0(\varepsilon)$ can be simplified to

$$\Delta\rho_0(\varepsilon) = \begin{cases} 0 & |\varepsilon| > V_2 \\ \frac{SV_2}{2\pi\gamma^2} & |\varepsilon| < V_2 \end{cases}. \quad (8)$$

From this equation, the LDOS of the bilayer graphene can be divided into two regions based on the interlayer hopping parameter V_2 . One region is $|\varepsilon| < V_2$, where the LDOS of site B is larger than that of site A by a constant, $\frac{SV_2}{2\pi\gamma^2}$. The other region is $|\varepsilon| > V_2$, where the LDOS of site A equals that of site B. Our calculations agree well with our numerical results when $V_2 = 0.4$ eV. The calculations show the dispersion relation is approximately quadratic dependent in the low-energy region and the results match the previous theoretical results.¹² We find that the low-energy LDOS of both sites A and B are linearly proportional to the energy (ε) (refer to the Appendix). Note that the LDOS of one unit cell at the very low-energy level, however, is a constant. The LDOS can be expressed as $\rho(\varepsilon) = [\rho_0(\mathbf{r}_A, \mathbf{r}_A, \varepsilon) + \rho_0(\mathbf{r}_B, \mathbf{r}_B, \varepsilon)] \simeq \frac{SV_2}{2\pi\gamma^2}$, which is the same as those in the conventional two-dimensional system. This remarkable feature of the bilayer graphene offers a direct method to measure the inter-layer hopping parameter V_2 , which is also the threshold needed to distinguish LDOS contrast in STM images. The intra-layer hopping parameter V_1 can be deduced based on the LDOS difference measured according to STM images ($\Delta\rho_0 = \frac{SV_2}{2\pi\gamma^2}$ with $\gamma = 3aV_1/2$).

III. LOCAL DENSITY OF STATES OF BILAYER GRAPHENE WITH LATTICE VACANCY

To validate the accuracy of real-space Green's function derived in this paper, we use the promoted formula to solve the electronic structure of a bilayer graphene with a single vacancy. Based on the tight-binding scheme, a vacancy can be simulated by introducing a large on-site energy at the vacancy site on a bilayer graphene.²³ Assuming that the single vacancy locates at site B with on-site energy U , the transport matrix or the T-matrix^{24,25} can be written as $T = U(1 - UG_0^{ret})^{-1}$. If U is large, the T-matrix becomes

$$\begin{aligned} T(0, 0, \varepsilon) &\simeq -G_0^{ret^{-1}}(0, 0, \varepsilon) \\ &= -F_2^{-1}(0, \varepsilon). \end{aligned} \quad (9)$$

Here, the position of the vacancy is set as the coordinate origin. That is to say, $\mathbf{R}_B = 0$ in the $x - y$ plane. Using the Dyson equation, we have

$$\begin{aligned} G^{ret}(\mathbf{r}_\mu, \mathbf{r}_\nu, \varepsilon) &= G_0^{ret}(\mathbf{r}_\mu, \mathbf{r}_\nu, \varepsilon) \\ &+ G_0^{ret}(\mathbf{r}_\mu, 0, \varepsilon)T(0, 0, \varepsilon)G_0^{ret}(0, \mathbf{r}_\nu, \varepsilon), \end{aligned} \quad (10)$$

where $G^{ret}(\mathbf{r}_\mu, \mathbf{r}_\nu, \varepsilon)$ is the Green's function of bilayer graphene with a single vacancy in real space. The LDOS on site \mathbf{r}_μ can be determined by

$$\rho(\mathbf{r}_\mu, \varepsilon) = -\frac{1}{\pi} \text{Im} G^{ret}(\mathbf{r}_\mu, \mathbf{r}_\mu, \varepsilon),$$

which can be simply rewritten as

$$\begin{aligned} \rho(\mathbf{r}_A, \varepsilon) &= \rho_0(\mathbf{r}_A, \varepsilon) + \sin^2(\mathbf{K}^1 \cdot \mathbf{r}_A + \alpha_{r_A})H_1(\mathbf{r}_A, \varepsilon), \\ \rho(\mathbf{r}_B, \varepsilon) &= \rho_0(\mathbf{r}_B, \varepsilon) + \cos^2(\mathbf{K}^1 \cdot \mathbf{r}_B)H_2(\mathbf{r}_B, \varepsilon). \end{aligned} \quad (11)$$

In the above equation,

$$\begin{aligned} \rho_0(\mathbf{r}_A, \varepsilon) &= -\frac{1}{\pi} \text{Im}[F_1(0, \varepsilon)], \\ \rho_0(\mathbf{r}_B, \varepsilon) &= -\frac{1}{\pi} \text{Im}[F_2(0, \varepsilon)], \\ H_1(\mathbf{r}_\mu, \varepsilon) &= \frac{1}{\pi} \text{Im}\left[\frac{F_3^2(|\mathbf{r}_\mu|, \varepsilon)}{F_2(0, \varepsilon)}\right], \\ H_2(\mathbf{r}_\mu, \varepsilon) &= \frac{1}{\pi} \text{Im}\left[\frac{F_2^2(|\mathbf{r}_\mu|, \varepsilon)}{F_2(0, \varepsilon)}\right]. \end{aligned} \quad (12)$$

Fig.4(a) shows the calculated LDOS with a single B-site vacancy on the top sheet of the bilayer graphene. An interesting feature is clearly observed; bright spots localized near the vacancy around site A have nice three-fold rotational symmetry. This phenomenon can be explained based on Eq.(11). Since the function H_2 in the Eq.(11) has a very small value (close to zero), its magnitude changes little as the distance from the vacancy increases and thus the magnitude of $\rho(\mathbf{r}_B, \varepsilon)$ remains very small. Although the cosine term in Eq.(11) reaches its maximum when $r_B = \frac{3\sqrt{3}a}{2}n$, $n = 0, \pm 1, \pm 2 \dots$, the sine function in $\rho(\mathbf{r}_A, \varepsilon)$ reaches its maximum along directions with angles, $\alpha_{r_A} = 30^\circ, 90^\circ, 150^\circ, 210^\circ, 270^\circ$ and 330° . Compared to H_2 , the value of the function H_1 has a relatively larger value, i.e. 0.4 eV^{-1} at 1.0 \AA away from the vacancy for $\varepsilon = -0.1 \text{ eV}$. The function H_1 , however, decays rapidly with increasing distance from the vacancy. Note that sites A along the directions $\alpha_{r_A} = 90^\circ, 210^\circ$ and 330° are located closer to the vacancy than those along the directions $\alpha_{r_A} = 30^\circ, 150^\circ$ and 270° . The calculated site-A LDOS value is between that of the nearest and that of the next nearest to the B-site vacancy, that is 0.56 eV^{-1} and 0.36 eV^{-1} , respectively. Therefore, the sites along the $\alpha_{r_A} = 90^\circ, 210^\circ$ and 330° directions are brighter than those along the $\alpha_{r_A} = 30^\circ, 150^\circ$ and 270° directions. These bright spots show the localized character of the region surrounding the vacancy. By comparing to the dI/dV image of a vacancy on the single-layer graphene¹⁹, the enhanced localization of LDOS in the bilayer graphene is caused by the additional inter-layer channel propagated from the vacancy point. Green's function can oscillate in a significantly longer distance starting from the vacancy in the monolayer graphene than in the bilayer graphene. The asymptotic behavior of H_1 can help us understand this phenomenon. When the distance is longer than 4.0 \AA , H_1 is less than 0.1 eV^{-1} and thus these bright spots show the localized character of the region within nearest lattice surrounding the vacancy.

The LDOS with vacancy near site-A is also simulated as shown in Fig. 4(b). We observe the similar features that the vacancy around site-B has bright spots with three-fold symmetry. The calculated site-B LDOS value is between that of the nearest and that of the next nearest to the site-A vacancy, which is between 0.35 eV^{-1} and 0.23 eV^{-1} .

The extension of our calculation to consider several vacancies on bilayer graphene is straightforward. The scattering T-matrix in Eq.(10) includes all contributions from vacancies. Similar to a single-vacancy case, a large on-site energy U for all vacancy sites is used in our simulations. Fig.4(c) shows the LDOS near an AB-type vacancy (a couple of

the neighboring sites A and B) on a bilayer graphene surface. The LDOS is still localized around the vacancies. However, the clear three-fold rotational symmetry disappears in this case. The bright spots localized above the vacancy correspond to the B sites. Note that the LDOS at the bright spots is about 0.03 eV^{-1} , which is less than those in Fig.4(a) and (b) by an order of magnitude. This phenomenon results in the destructive interference due to the multiple-scattering caused by two vacancies. The asymmetric pattern in Fig. 4(c) reflects the residual contribution from the destructive interference since two sites A and B are nonequivalent in the bilayer graphene. Our result suggests that the interference pattern is determined mainly by vacancies, provided that the spatial anisotropy of the Green's function is fixed. The symmetry will be lost in LDOS whenever vacancies break the three-fold rotational symmetry in bilayer graphene.

IV. CONCLUSION

In this paper, an analytical form of the real-space Green's function (propagator) of bilayer graphene is constructed based on the effective-mass approximation. Green's function demonstrates an elegant spatial anisotropy with a three-fold symmetry for defect-free bilayer graphene. The LDOS of the bilayer graphene determines the main features of experimental STM images on graphite surfaces with low-bias voltage. The predicted features according to our simulated results can be verified by STM measurements. For example, two nonequivalent atomic sites can be observed in STM dI/dV images with different bias voltages. The information of interlayer and intralayer hopping strength can be deduced based on the contrast of STM images. Moreover, We also calculate the LDOS of bilayer graphene with vacancies by using the multiple-scattering theory. The interference patterns are determined mainly by the properties of Green's function and the symmetry of the vacancies. Once the vacancies break the intrinsic symmetry of the graphene, the three-fold rotational symmetry of the LDOS vanishes. Our model provides exact results near the Dirac points. We have discovered some interesting STM patterns of the second layer, but these results will be published elsewhere. In this paper, the bilayer graphene is described by using the simple non-interactive tight-binding scheme. We are currently investigating how Coulomb interaction impacts the electronic structure of the bilayer graphene.

ACKNOWLEDGMENTS

This work is partially supported by the National Natural Science Foundation of China under Grants 10274076, 10674121, 20533030, 20303015 and 50121202, by National Key Basic Research Program under Grant No. 2006CB0L1200, by the USTC-HP HPC project, and by the SCCAS and Shanghai Supercomputer Center. Work at NTU is supported in part by COE-SUG grant (No. M58070001). Jie Chen would like to acknowledge the funding support from the Discovery program of Natural Sciences and Engineering Research Council of Canada (No. 245680).

APPENDIX

From Eq.(3), Green's functions at the top layer in reciprocal space are expressed as

$$\begin{aligned}
 G_{0AA}^{ret}(\mathbf{k}, \varepsilon) &= \frac{1}{2} \left[\frac{t}{t^2 - V_1^2 \mu \mu^* - tV_2} + \frac{t}{t^2 - V_1^2 \mu \mu^* + tV_2} \right] \\
 G_{0BB}^{ret}(\mathbf{k}, \varepsilon) &= \frac{1}{2} \left[\frac{t - V_2}{t^2 - V_1^2 \mu \mu^* - tV_2} + \frac{t + V_2}{t^2 - V_1^2 \mu \mu^* + tV_2} \right] \\
 G_{0AB}^{ret}(\mathbf{k}, \varepsilon) &= \frac{1}{2} \left[\frac{V_1 \mu^*}{t^2 - V_1^2 \mu \mu^* - tV_2} + \frac{V_1 \mu^*}{t^2 - V_1^2 \mu \mu^* + tV_2} \right] \\
 G_{0BA}^{ret}(\mathbf{k}, \varepsilon) &= \frac{1}{2} \left[\frac{V_1 \mu}{t^2 - V_1^2 \mu \mu^* - tV_2} + \frac{V_1 \mu}{t^2 - V_1^2 \mu \mu^* + tV_2} \right]
 \end{aligned} \tag{A-1}$$

By taking the Fourier transform of $G_{0\mu\nu}^{ret}(\mathbf{k}, \varepsilon)$ in the first Brillouin zone (1BZ), we can obtain the exact expression of Green's function in real space for bilayer graphene $G_0^{ret}(\mathbf{r}_\mu, \mathbf{r}'_\nu, \varepsilon) = \int_{1BZ} d\mathbf{k} G_{0\mu\nu}^{ret}(\mathbf{k}, \varepsilon) e^{i\mathbf{k} \cdot (\mathbf{r}_\mu - \mathbf{r}'_\nu)}$, where μ and ν are for site-A or site-B atoms, respectively. Based on the effective-mass approximation, we can sum k points near the six corners (labeled by $i = 1 \sim 6$) in the first Brillouin zone. The real-space bilayer graphene Green's function can

be written as

$$\begin{aligned}
G_0^{ret}(\mathbf{r}_A, \mathbf{r}'_A, \varepsilon) &= \frac{S}{(2\pi)^2} \sum_{i=1}^6 \int dk_x^i dk_y^i \left[\frac{t}{t^2 - V_1^2 \mu_i \mu_i^* - tV_2} + \frac{t}{t^2 - V_1^2 \mu_i \mu_i^* + tV_2} \right] e^{i(\mathbf{K}^i + \mathbf{k}^i) \cdot (\mathbf{r}_A - \mathbf{r}'_A)} \\
G_0^{ret}(\mathbf{r}_B, \mathbf{r}'_B, \varepsilon) &= \frac{S}{(2\pi)^2} \sum_{i=1}^6 \int dk_x^i dk_y^i \left[\frac{t - V_2}{t^2 - V_1^2 \mu_i \mu_i^* - tV_2} + \frac{t + V_2}{t^2 - V_1^2 \mu_i \mu_i^* + tV_2} \right] e^{i(\mathbf{K}^i + \mathbf{k}^i) \cdot (\mathbf{r}_B - \mathbf{r}'_B)} \\
G_0^{ret}(\mathbf{r}_A, \mathbf{r}'_B, \varepsilon) &= \frac{S}{(2\pi)^2} \sum_{i=1}^6 \int dk_x^i dk_y^i \left[\frac{V_1 \mu_i^*}{t^2 - V_1^2 \mu_i \mu_i^* - tV_2} + \frac{V_1 \mu_i^*}{t^2 - V_1^2 \mu_i \mu_i^* + tV_2} \right] e^{i(\mathbf{K}^i + \mathbf{k}^i) \cdot (\mathbf{r}_A - \mathbf{r}'_B)} \\
G_0^{ret}(\mathbf{r}_B, \mathbf{r}'_A, \varepsilon) &= \frac{S}{(2\pi)^2} \sum_{i=1}^6 \int dk_x^i dk_y^i \left[\frac{V_1 \mu_i}{t^2 - V_1^2 \mu_i \mu_i^* - tV_2} + \frac{V_1 \mu_i}{t^2 - V_1^2 \mu_i \mu_i^* + tV_2} \right] e^{i(\mathbf{K}^i + \mathbf{k}^i) \cdot (\mathbf{r}_B - \mathbf{r}'_A)}
\end{aligned} \tag{A-2}$$

In Eq.(A-2), the integral around K^1, K^3, K^5 and K^2, K^4, K^6 can be summed together separately to form two 360° integrals around K^1 and K^4 , that is

$$\begin{aligned}
G_0^{ret}(\mathbf{r}_A, \mathbf{r}'_A, \varepsilon) &= \frac{S}{(2\pi)^2} [e^{i\mathbf{K}^1(\mathbf{r}_A - \mathbf{r}'_A)} + e^{i\mathbf{K}^4(\mathbf{r}_A - \mathbf{r}'_A)}] \\
&\quad \times \int_0^{2\pi} d\theta \int_0^{k_c} dk k \left[\frac{t}{t^2 - (\gamma k)^2 - tV_2} + \frac{t}{t^2 - (\gamma k)^2 + tV_2} \right] e^{i\mathbf{k} \cdot (\mathbf{r}_A - \mathbf{r}'_A)} \\
G_0^{ret}(\mathbf{r}_B, \mathbf{r}'_B, \varepsilon) &= \frac{S}{(2\pi)^2} [e^{i\mathbf{K}^1(\mathbf{r}_B - \mathbf{r}'_B)} + e^{i\mathbf{K}^4(\mathbf{r}_B - \mathbf{r}'_B)}] \\
&\quad \times \int_0^{2\pi} d\theta \int_0^{k_c} dk k \left[\frac{t - V_2}{t^2 - (\gamma k)^2 - tV_2} + \frac{t + V_2}{t^2 - (\gamma k)^2 + tV_2} \right] e^{i\mathbf{k} \cdot (\mathbf{r}_B - \mathbf{r}'_B)} \\
G_0^{ret}(\mathbf{r}_A, \mathbf{r}'_B, \varepsilon) &= \frac{S}{(2\pi)^2} \{ e^{i\mathbf{K}^1(\mathbf{r}_A - \mathbf{r}'_B)} \\
&\quad \times \int_0^{2\pi} d\theta \int_0^{k_c} dk k^2 \gamma (-i \sin \theta - \cos \theta) \left[\frac{1}{t^2 - (\gamma k)^2 - tV_2} + \frac{1}{t^2 - (\gamma k)^2 + tV_2} \right] e^{i\mathbf{k} \cdot (\mathbf{r}_A - \mathbf{r}'_B)} \\
&\quad + e^{i\mathbf{K}^4(\mathbf{r}_A - \mathbf{r}'_B)} \\
&\quad \times \int_0^{2\pi} d\theta \int_0^{k_c} dk k^2 \gamma (-i \sin \theta + \cos \theta) \left[\frac{1}{t^2 - (\gamma k)^2 - tV_2} + \frac{1}{t^2 - (\gamma k)^2 + tV_2} \right] e^{i\mathbf{k} \cdot (\mathbf{r}_A - \mathbf{r}'_B)} \} \\
G_0^{ret}(\mathbf{r}_B, \mathbf{r}'_A, \varepsilon) &= \frac{S}{(2\pi)^2} \{ e^{i\mathbf{K}^1(\mathbf{r}_B - \mathbf{r}'_A)} \\
&\quad \times \int_0^{2\pi} d\theta \int_0^{k_c} dk k^2 \gamma (i \sin \theta - \cos \theta) \left[\frac{1}{t^2 - (\gamma k)^2 - tV_2} + \frac{1}{t^2 - (\gamma k)^2 + tV_2} \right] e^{i\mathbf{k} \cdot (\mathbf{r}_B - \mathbf{r}'_A)} \\
&\quad + e^{i\mathbf{K}^4(\mathbf{r}_B - \mathbf{r}'_A)} \int_0^{2\pi} d\theta \\
&\quad \times \int_0^{k_c} dk k^2 \gamma (i \sin \theta + \cos \theta) \left[\frac{1}{t^2 - (\gamma k)^2 - tV_2} + \frac{1}{t^2 - (\gamma k)^2 + tV_2} \right] e^{i\mathbf{k} \cdot (\mathbf{r}_B - \mathbf{r}'_A)} \}
\end{aligned} \tag{A-3}$$

By using relation

$$e^{i\mathbf{k} \cdot (\mathbf{r}_\mu - \mathbf{r}'_\nu)} = J_0(k|\mathbf{r}_\mu - \mathbf{r}'_\nu|) + 2 \sum_{n=1}^{\infty} i^n J_n(k|\mathbf{r}_\mu - \mathbf{r}'_\nu|) \cos(n\varphi_{r_\mu, r'_\nu}),$$

and integrating the angle part of Eq.(A-3), we can easily get Eqs.(4) and (5). If we let $k_c \rightarrow \infty$, Eq.(5) is simplified to Eq.(6).

Next, we briefly derive Eq.(8). At the same site A or B, the corresponding Green's functions are:

$$\begin{aligned} G_0^{ret}(\mathbf{r}_A, \mathbf{r}_A, \varepsilon) &= \frac{S}{\pi} \int_0^{k_c} dk k \left[\frac{t}{t^2 - (\gamma k)^2 - tV_2} + \frac{t}{t^2 - (\gamma k)^2 + tV_2} \right], \\ G_0^{ret}(\mathbf{r}_B, \mathbf{r}_B, \varepsilon) &= \frac{S}{\pi} \int_0^{k_c} dk k \left[\frac{t - V_2}{t^2 - (\gamma k)^2 - tV_2} + \frac{t + V_2}{t^2 - (\gamma k)^2 + tV_2} \right]. \end{aligned} \quad (\text{A-4})$$

The LDOS at sites A and B are

$$\begin{aligned} \rho_0(\mathbf{r}_A, \mathbf{r}_A, \varepsilon) &= -\frac{1}{\pi} \text{Im}[G_0^{ret}(\mathbf{r}_A, \mathbf{r}_A, \varepsilon)] \\ &= -\frac{S}{2(\pi\gamma)^2} \text{Im} \int_0^{k_c} d[\sqrt{(\gamma k)^2 + (\frac{V_2}{2})^2}] \\ &\quad \left\{ \frac{t}{\varepsilon + i\eta - \frac{V_2}{2} - \sqrt{(\gamma k)^2 + (\frac{V_2}{2})^2}} - \frac{t}{\varepsilon + i\eta - \frac{V_2}{2} + \sqrt{(\gamma k)^2 + (\frac{V_2}{2})^2}} + \right. \\ &\quad \left. \frac{t}{\varepsilon + i\eta + \frac{V_2}{2} - \sqrt{(\gamma k)^2 + (\frac{V_2}{2})^2}} - \frac{t}{\varepsilon + i\eta + \frac{V_2}{2} + \sqrt{(\gamma k)^2 + (\frac{V_2}{2})^2}} \right\} \\ &= \begin{cases} \frac{S|\varepsilon|}{\pi\gamma^2} & |\varepsilon| > V_2 \\ \frac{S|\varepsilon|}{2\pi\gamma^2} & |\varepsilon| < V_2 \end{cases}. \end{aligned} \quad (\text{A-5})$$

$$\begin{aligned} \rho_0(\mathbf{r}_B, \mathbf{r}_B, \varepsilon) &= -\frac{1}{\pi} \text{Im}[G_0^{ret}(\mathbf{r}_B, \mathbf{r}_B, \varepsilon)] \\ &= -\frac{S}{2(\pi\gamma)^2} \text{Im} \int_0^{k_c} d[\sqrt{(\gamma k)^2 + (\frac{V_2}{2})^2}] \\ &\quad \left\{ \frac{t - V_2}{\varepsilon + i\eta - \frac{V_2}{2} - \sqrt{(\gamma k)^2 + (\frac{V_2}{2})^2}} - \frac{t - V_2}{\varepsilon + i\eta - \frac{V_2}{2} + \sqrt{(\gamma k)^2 + (\frac{V_2}{2})^2}} + \right. \\ &\quad \left. \frac{t + V_2}{\varepsilon + i\eta + \frac{V_2}{2} - \sqrt{(\gamma k)^2 + (\frac{V_2}{2})^2}} - \frac{t + V_2}{\varepsilon + i\eta + \frac{V_2}{2} + \sqrt{(\gamma k)^2 + (\frac{V_2}{2})^2}} \right\} \\ &= \begin{cases} \frac{S|\varepsilon|}{\pi\gamma^2} & |\varepsilon| > V_2 \\ \frac{S(|\varepsilon| + V_2)}{2\pi\gamma^2} & |\varepsilon| < V_2 \end{cases}. \end{aligned} \quad (\text{A-6})$$

Then, the difference between LDOS at A and B sites is

$$\begin{aligned}\Delta\rho_0(\varepsilon) &= \rho_0(\mathbf{r}_B, \mathbf{r}_B, \varepsilon) - \rho_0(\mathbf{r}_A, \mathbf{r}_A, \varepsilon) \\ &= \begin{cases} 0 & |\varepsilon| > V_2 \\ \frac{SV_2}{2\pi\gamma^2} & |\varepsilon| < V_2 \end{cases}.\end{aligned}\tag{A-7}$$

* Corresponding author. E-mail: liquan@ustc.edu.cn

† Corresponding author. E-mail: phsqw@ustc.edu.cn

- ¹ K. S. Novoselov, A. K. Geim, S. V. Morozov, D. Jiang, M. I. Katsnelson, I. V. Grigorieva, S. V. Dubonos, and A. A. Firsov, *Nature* **438**,197 (2005).
- ² T. Matsui, H. Kambara, Y. Niimi, K. Tagami, M. Tsukada, and Hiroshi Fukuyama, *Phys. Rev. Lett.* **94**,226403 (2005).
- ³ Vitor M. Pereira, F. Guinea, J. M. B. Lopes dos Santos, N. M. R. Peres, and A. H. Castro Neto, *Phys. Rev. Lett.* **96**,036801 (2006).
- ⁴ J. Tworzydło, B. Trauzettel, M. Titov, A. Rycerz, and C.W. J. Beenakker, *Phys. Rev. Lett.* **96**,246802 (2006).
- ⁵ N. M. R. Peres, F. Guinea, and A. H. Castro Neto, *Phys. Rev. B* **73**,125411 (2006).
- ⁶ Y. Zhang, Z. Jiang, J. P. Small, M. S. Purewal, Y.-W. Tan, M. Fazlollahi, J. D. Chudow, J. A. Jaszczak, H. L. Stormer, and P. Kim, *Phys. Rev. Lett.* **96**,136806 (2006).
- ⁷ Dmitry A. Abanin, Patrick A. Lee, and Leonid S. Levitov, *Phys. Rev. Lett.* **96**,176803 (2006).
- ⁸ Claire Berger, Zhimin Song, Tianbo Li, Xuebin Li, Asmerom Y. Ogbazghi, Rui Feng, Zhenting Dai, Alexei N. Marchenkov, Edward H. Conrad, Phillip N. First, and Walt A. de Heer, *J. Phys. Chem. B* **108**, 19912 (2004).
- ⁹ Claire Berger, Zhimin Song, Xuebin Li, Xiaosong Wu, Nate Brown, Cécile Naud, Didier Mayou, Tianbo Li, Joanna Hass, Alexei N. Marchenkov, Edward H. Conrad, Phillip N. First, and Walt A. de Heer, *Science* **312**, 1191 (2006)
- ¹⁰ Johan Nilsson, A. H. Castro Neto, F. Guinea, N. M. R. Peres, cond-mat/0604106.
- ¹¹ K. S. Novoselov, E. McCaen, S. V. Morozov, V. I. Fal'ko, M. I. Katsnelson, U. Zeitler, D. Jiang, F. Schedin, A. K. Geim, *Nature Phys.* **2**,177 (2006).
- ¹² Edward McCann and Vladimir I. Fal'ko, *Phys. Rev. Lett.* **96**,086805 (2006).
- ¹³ Mikito Koshino and Tsuneya Ando, *Phys. Rev. B* **73**,245403 (2006).

- ¹⁴ Johan Nilsson, A. H. Castro Neto, F. Guinea, N. M. R. Peres, cond-mat/0607343.
- ¹⁵ M. I. Katsnelson, K. S. Novoselov, A. K. Geim, Nature Phys. **2**, 620 (2006).
- ¹⁶ David Tománek, Steven G. Louie, H. Jonathon Mamin, David W. Abraham, Ruth Ellen Thomson, Eric Ganz, and John Clarke, Phys. Rev. B **35**,7790 (1987).
- ¹⁷ Stefan Hembacher, Franz J. Giessibl, Jochen Mannhart, and Calvin F. Quate, Proc. Natl. Acad. Sci. U.S.A. **100**, 12539 (2003).
- ¹⁸ Yongfeng Wang, Yingchun Ye, Kai Wu, Surf. Sci. **600**,729 (2006).
- ¹⁹ Z. F. Wang, Ruoxi Xiang, Q. W. Shi, Jinlong Yang, Xiaoping Wang, J. G. Hou, and Jie Chen, Phys. Rev. B **74**, 125417 (2006).
- ²⁰ J. Tersoff and D. R. Hamann, Phys. Rev. B **31**, 805 (1985).
- ²¹ J. G. Hou, Jinlong Yang, Haiqian Wang, Qunxiang Li, Changgan Zeng, Hai Lin, Bing Wang, D. M. Chen, and Qingshi Zhu, Phys. Rev. Lett. **83**, 3001 (1999); J.G.Hou, Jinlong Yang, Haiqian Wang, Qunxiang Li, Changgan Zeng, Lanfeng Yuan, Bing Wang, D. M. Chen, Qingshi Zhu, Nature **409**, 304 (2001); Aidi Zhao, Qunxiang Li, Lan Chen, Hongjun Xiang, Weihua Wang, Shuan Pan, Bing Wang, Jinlong Yang, J. G. Hou, and Qingshi Zhu, Science **309** 1542 (2005).
- ²² Qunxiang Li and Xiao Hu, Phys. Rev. B **74**, 035414 (2006).
- ²³ Tsuneya Ando, Takeshi Nakanishi and Masatsura Igami, J. Phys. Soc. Jpn. **68**, 3994 (1999).
- ²⁴ Qiang-Hua Wang and Dung-Hai Lee, Phys. Rev. B **67**,020511(R) (2003).
- ²⁵ J. M. Byers, M. E. Flatté, and D. J. Scalapino, Phys. Rev. Lett. **71**,3363 (1993).

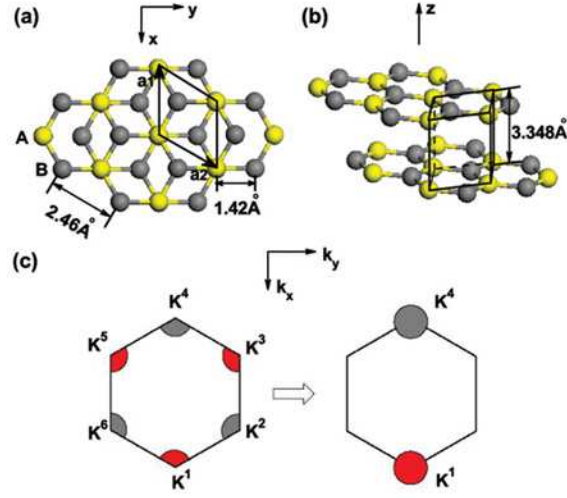


Figure 1: (color online) The crystal structure of a bilayer graphene. The unit cell consists of two layers with two nonequivalent sites: A (yellow) and B (gray). (a) Top view with surface unit vectors a_1 and a_2 , (b) Side view. (c) The first Brillouin zone of a bilayer graphene, where $K^1 \sim K^6$ are the Dirac points. These Dirac points can be further divided into two nonequivalent sets, $K^1 \sim (K^1, K^3, K^5)$ and $K^4 \sim (K^2, K^4, K^6)$.

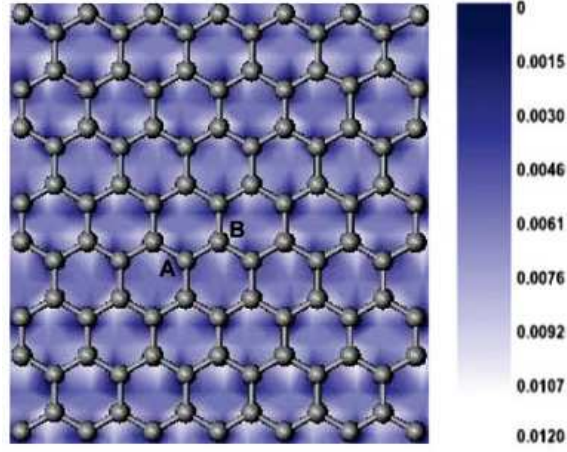


Figure 2: (color online) LDOS of bilayer graphene with $\varepsilon = -0.1$ eV. The LDOS at B site is larger than that at A site, represented by the brighter contour.

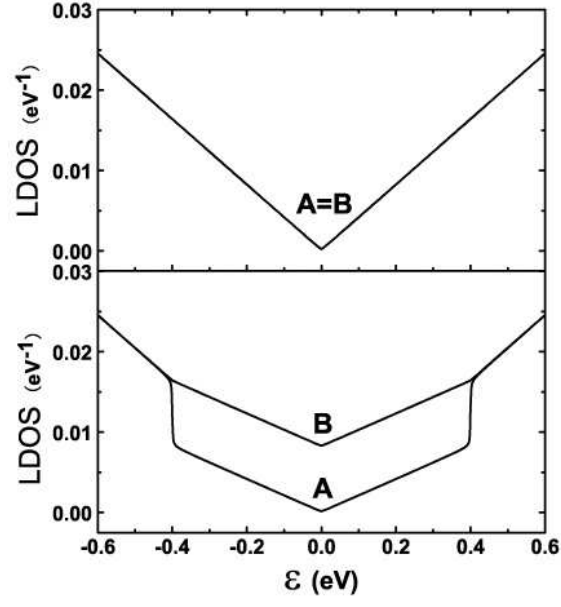


Figure 3: (a) LDOS of monolayer graphene on one site (sites A and B are equivalent). (b) LDOS of bilayer graphene on two sites (sites A and B are nonequivalent).

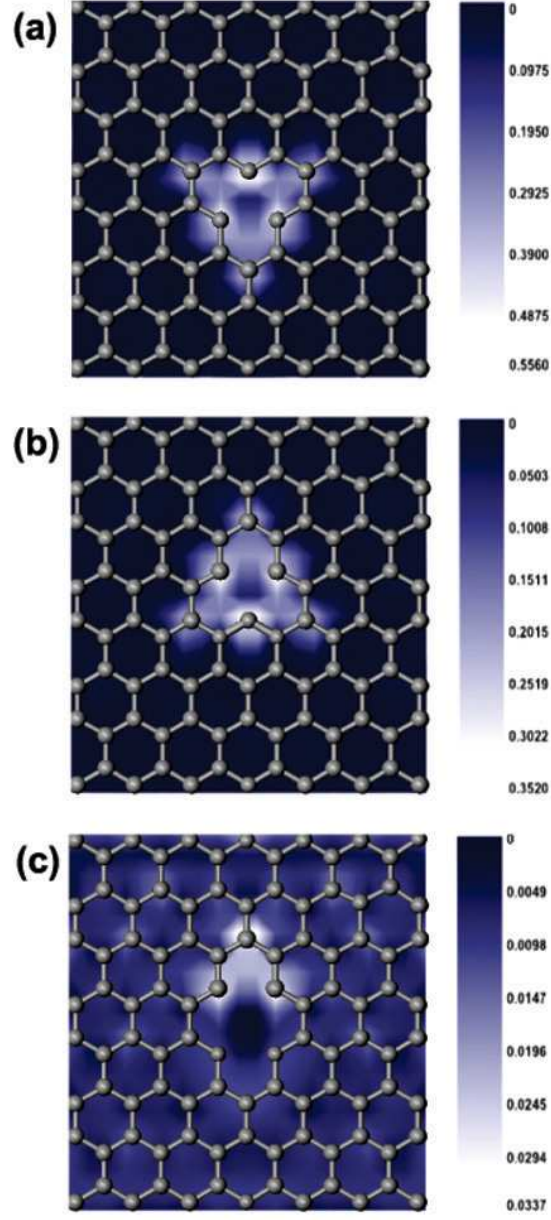


Figure 4: (color online) LDOS of vacancies in bilayer graphene. (a) single B-site vacancy; (b) A-site vacancy; (c) a pair of AB vacancy. Here, $\varepsilon = -0.1$ eV